AGU PUBLICATIONS

JGR

Journal of Geophysical Research: Atmospheres

RESEARCH ARTICLE
10.1002/2013JD021208

Key Points:
- CO_2 and CO are simulated in the mesosphere and lower thermosphere (MLT)
- Calculations agree with a variety of satellite observations
- There appear to be no major deficiencies in the current understanding of CO_2 and CO in the MLT

Correspondence to:
R. R. Garcia,
rgarcia@ucar.edu

Citation:
Garcia, R. R., M. López-Puertas, B. Funke, D. R. Marsh, D. E. Kinnison, A. K. Smith, and F. González-Galindo (2014), On the distribution of CO_2 and CO in the mesosphere and lower thermosphere, *J. Geophys. Res. Atmos.*, *119*, 5700–5718, doi:10.1002/2013JD021208.

Received 15 NOV 2013
Accepted 10 APR 2014
Accepted article online 13 APR 2014
Published online 13 MAY 2014

On the distribution of CO_2 and CO in the mesosphere and lower thermosphere

Rolando R. Garcia[1], Manuel López-Puertas[2], Bernd Funke[2], Daniel R. Marsh[1], Douglas E. Kinnison[1], Anne K. Smith[1], and Francisco González-Galindo[2]

[1]National Center for Atmospheric Research, Boulder, Colorado, USA, [2]Instituto de Astrofísica de Andalucía, CSIC, Granada, Spain

Abstract We have used the Whole Atmosphere Community Climate Model (WACCM) to calculate the distribution of CO_2 and CO in the mesosphere and lower thermosphere (MLT), and we have compared the results with observations, mainly from the Atmospheric Chemistry Experiment Fourier Transform Spectrometer and Michelson Interferometer for Passive Atmospheric Sounding satellite-borne instruments. We find that WACCM can reproduce the observed distribution of CO_2 in the MLT and the rapid falloff of CO_2 above about 80 km. Analysis of the principal terms in the calculated budget of CO_2 shows that its global-mean vertical profile is determined mainly by the competition between molecular diffusive separation and eddy mixing by gravity waves. The model underestimates somewhat the mixing ratio of CO_2 in the thermosphere compared to that in the observations, but we show that the discrepancy may be eliminated by a reasonable adjustment of the Prandtl number used to calculate the diffusivity due to gravity waves. Simulated CO is also consistent with observations, except that in the standard version of the model, its mixing ratio is uniformly lower than observed above about 100 km. We conclude that WACCM likely underestimates the rate of production of CO in the lower thermosphere from photolysis of CO_2 at wavelengths < 121 nm, and we show that this stems from the use of a very large absorption cross section for O_2 in the wavelength range 105–121 nm. When a smaller cross section is used, photolysis of CO_2 increases by a factor of 2–3 at ~95–115 km and, as a result, CO mixing ratios become larger and agree much more closely with observations. We emphasize that the increase in CO_2 photolysis implies only minor changes in the vertical profile of CO_2 because photolytic loss is a minor term in the budget of CO_2 in the MLT.

1. Introduction

Carbon dioxide, CO_2, is a minor constituent of the atmosphere that is well mixed from the troposphere to the upper mesosphere. Above about 80 km, its mixing ratio begins to decrease due to diffusive separation (CO_2 is heavier than the mean molecular weight of air) and photodissociation [*Chabrillat et al.*, 2002]. Infrared emission by CO_2 is the major cooling mechanism of the mesosphere and lower thermosphere [see, e.g., *López-Puertas and Taylor*, 2001; *Mlynczak et al.*, 2008], and observations of CO_2 emissions in various bands are widely used for remote sounding of the temperature and composition of the atmosphere. However, CO_2 measurements in the mesosphere and lower thermosphere (MLT) are scarce, and no global observations have been made until recently. *López-Puertas et al.* [2000] have reviewed the CO_2 measurements taken before 2000.

Several recently developed instruments offer the possibility of measuring CO_2 on a near-global basis. For example, the Michelson Interferometer for Passive Atmospheric Sounding (MIPAS) [*Fischer et al.*, 2008] is capable of retrieving CO_2 from 10 μm and 4.3 μm emissions in the middle atmosphere, although observations have been made only for relatively short periods in the last few years. The SABER (Sounding of the Atmosphere by Broadband Emission Radiometry) instrument on NASA's TIMED (Thermosphere-Ionosphere-Mesosphere Radiation and Dynamics) satellite can retrieve CO_2 over a broad range of altitude in sunlit conditions, but thus far, only preliminary CO_2 distributions have been derived from SABER [*Mertens et al.*, 2009]. Measurements of CO_2 have also been made recently by the Fourier Transform Spectrometer on the Canadian Atmospheric Chemistry Experiment satellite (ACE), and these observations are now available over a period of several years [*Beagley et al.*, 2010].

The observations of CO_2 in the middle atmosphere summarized by *López-Puertas et al.* [2000] show a rapid falloff above about 80 km, which could not be reproduced well by the one- and two-dimensional models reviewed by these authors. López-Puertas et al. performed a model sensitivity study in a globally averaged, one-dimensional model to show that eddy diffusion plays a key role in producing the observed falloff of CO_2,

such that agreement in observed and calculated vertical profiles of CO_2 could be obtained only if the eddy diffusion coefficient used in the model was sufficiently small (in the range of about 10 $m^2 s^{-1}$ in the upper mesosphere to 100 $m^2 s^{-1}$ in the lower thermosphere). *Chabrillat et al*. [2002] demonstrated the importance of including molecular diffusive separation, which opposes the effect of vertical mixing by eddy diffusion, in the calculation of the distribution of CO_2 in the MLT.

The recent availability of measurements from the ACE and MIPAS instruments mentioned above has confirmed the rapid falloff of CO_2 near 80 km and raised the question whether currently available three-dimensional (3-D) models of the atmosphere with coupled chemistry are capable of simulating the observed behavior of CO_2. *Beagley et al*. [2010] compared ACE measurements of CO_2 and CO with 3-D simulations made with the Canadian Middle Atmosphere Model (CMAM) and concluded that CMAM could not reproduce the observed falloff of CO_2 with altitude using standard photochemical loss mechanisms, even though CMAM presumably includes the other physical processes that are believed to be important in the MLT, eddy and molecular diffusion. Furthermore, when they artificially increased the rate of CO_2 photolysis to produce a vertical profile of CO_2 in agreement with observations, they found that the calculated abundance of carbon monoxide, CO, was much larger than observed. Beagley et al. therefore speculated that sequestration of CO_2 on meteoritic dust might be required to explain the observed vertical profile of CO_2, as such a process would reduce the abundance of CO_2 without increasing CO.

In this study, we compare recent measurements of CO_2 by ACE, CO by ACE and MIPAS, and various other observations of these two species with simulations made with the Whole Atmosphere Community Climate Model. Additional loss mechanisms for CO_2 (photolysis at extreme ultraviolet wavelengths and reaction with O^+) have been identified and included in the simulations. We demonstrate that these additions improve the calculation of CO without, however, materially affecting the vertical profile of CO_2. We conclude by discussing the strengths and the deficiencies of the model and show that the latter can be remedied by adjustment of the parameters that control the calculation of eddy diffusion and of the photolysis rate of CO_2 at wavelengths < 121 nm.

2. The Numerical Model

The Whole Atmosphere Community Climate Model (WACCM) is a comprehensive chemistry-climate model that covers the altitude range 0–140 km. An earlier version of the model was described in detail by *Garcia et al*. [2007]. The current version of WACCM (version 4) is similar to that described by Garcia et al., except that model chemistry has been updated to be consistent with Jet Propulsion Laboratory 2010 recommendations [*Sander et al*., 2011]; additional loss mechanisms for CO_2 have been included, as discussed below, and the gravity wave parameterization has been updated, such that the time and spatial dependence of the source spectra are now dependent on model-calculated fields (convective heat release in the tropics and diagnosis of frontal zones in extratropical latitudes; see *Richter et al*. [2010]). Other significant changes include the generation of a quasi-biennial oscillation by relaxation of stratospheric tropical winds to observations [*Matthes et al*., 2004] and the parameterization of heating by stratospheric volcanic aerosols. However, these changes are not particularly important for modeling CO and CO_2 above the mesopause. A detailed description of the current version of WACCM is given by *Marsh et al*. [2013].

Version 4 of WACCM also provides the option of constraining the winds and temperature everywhere below ~1 hPa using reanalysis data. The model is free running above this altitude, but as discussed by *Liu et al*. [2009], the dynamics of the mesosphere and lower thermosphere are strongly constrained by the behavior of the lower atmosphere. This "specified dynamics" version of the model, denominated SD-WACCM, is used in the present work because it provides the ability to compare more closely the model results with observations made by ACE and MIPAS. In particular, we compare results for years near solar minimum, 2007–2009, with ACE and MIPAS observations available for that period, as detailed in section 3. In these simulations, SD-WACCM is constrained with output from NASA's Modern-Era Retrospective Analysis (MERRA) [*Rienecker et al*., 2011] using the procedure discussed in detail by *Kunz et al*. [2011].

The model uses zero-flux conditions for both CO and CO_2 at the upper boundary. Previous versions of WACCM employed specified mixing ratios, taken from the National Center for Atmospheric Research's (NCAR's) thermosphere-ionosphere-mesosphere-electrodynamics general circulation model (TIME-GCM) model [*Roble and Ridley*, 1994], which is inconvenient as it requires repeating TIME-GCM calculations as CO_2 changes due to anthropogenic emissions or as CO and CO_2 change due to solar variability. We have

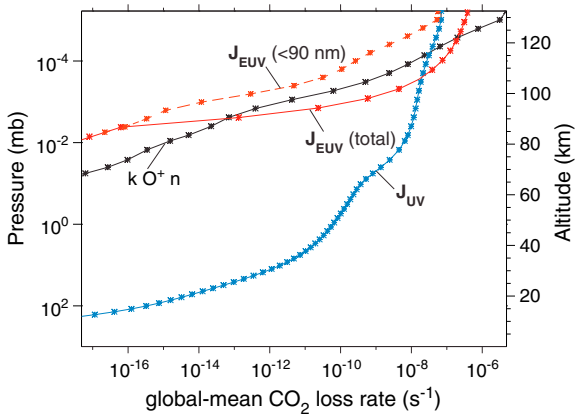

Figure 1. Global-mean profiles of the CO_2 loss rate (s^{-1}) due to different processes, for equinox conditions. Loss by reaction with the atomic oxygen ion is denoted by $k\ O^+\ n$. Loss due to UV and EUV radiation is denoted by J_{UV} and J_{EUV}, respectively. J_{EUV} (<90 nm) is the partial loss rate due to EUV radiation in the wavelength range 0–90 nm. See text for details.

ascertained by comparison of WACCM simulations with either zero flux or specified concentration at the upper boundary that the solution for CO and CO_2 is not affected by the choice of boundary condition below about 10^{-4} hPa, the highest altitude considered in this study.

In addition to photolysis of CO_2 at ultraviolet wavelengths, 121–200 nm, for which we use the cross sections documented by *Thompson et al.* [1963] and solar fluxes from the Naval Research Laboratory Solar Spectral Irradiance model [*Lean et al.*, 2005], we have included in our calculations two loss mechanisms for CO_2 that were not present in earlier versions of WACCM. The first is photolysis of CO_2 in the extreme ultraviolet (EUV),

$$CO_2 + h\nu \rightarrow CO + O \qquad (\lambda < 121\ \text{nm}), \quad (1)$$

where the EUV flux is parameterized as a function of the 10.7 cm radio flux by the method of *Solomon and Qian* [2005], and the absorption cross section of CO_2 is taken from *Huestis and Berkowitz* [2010]. The second loss mechanism is the reaction of CO_2 with the atomic oxygen ion,

$$CO_2 + O^+ \rightarrow CO + O_2{}^+ \qquad \left(k = 9 \times 10^{-10}\,\text{cm}^3\,\text{s}^{-1}\right), \quad (2)$$

where the reaction rate coefficient, k, is taken from *Lindinger et al.* [1974]. Figure 1 compares the loss rates of CO_2 due to EUV absorption, J_{EUV} (1), and reaction with O^+ (2) with the loss due to photolysis at ultraviolet (UV) wavelengths longward of 121 nm, J_{UV}. Below 10^{-3} hPa (~100 km), the loss rates from (1) and (2) are negligible compared to J_{UV}, but the reverse is true at higher altitudes. Nevertheless, a calculation where CO_2 loss via (1) and (2) is not included (not shown) indicates that these losses reduce the global-mean mixing ratio of CO_2 by less than 10% above 100 km. This occurs because the global-mean vertical profile of CO_2 in WACCM is determined principally by the competition between eddy diffusion due to dissipating gravity waves and diffusive separation of CO_2 and not by photolytic or chemical loss [cf. *Chabrillat et al.*, 2002]. This point is illustrated and discussed in detail in section 5.

We note that in our calculations (1) is assumed to produce CO at all wavelengths; however, absorption by CO_2 of radiation shortward of ~90 nm (the ionization threshold) leads to various ionized products rather than to dissociation into CO and O. This overestimates the rate of production of CO from J_{EUV} shortward of 90 nm, but the error is insignificant, for two reasons: First, over 60% of the ionized CO_2 eventually produces CO, as may be deduced from the reaction rates listed in *Nagy et al.* [1980, Table 1] and the ratio of $CO_2{}^+$ to CO^+ ion production given by *Fox and Dalgarno* [1979], and, second, radiation shortward of 90 nm dominates the production rate of CO from J_{EUV} only near 0.01 hPa (80–90 km), but at those altitudes J_{EUV} is negligible compared to J_{UV}. At altitudes above 100 km, where J_{EUV} becomes faster than J_{UV}, J_{EUV} (< 90 nm) is small compared to the total J_{EUV}. These points are illustrated by the dashed curve in Figure 1, which also shows J_{EUV} (<90 nm) in comparison to the other CO_2 loss processes.

Molecular and eddy diffusion are of central importance for calculating the abundance of CO_2 in the mesosphere and lower thermosphere. The treatment of molecular diffusion in WACCM follows the "minor constituent" formulation [*Banks and Kockarts*, 1973, chapter 15]. In brief, the contribution of molecular diffusion to the time rate of change of a minor species is given by [*Smith et al.*, 2011]:

$$\frac{\partial \chi_i}{\partial t} = \frac{1}{\rho}\frac{\partial}{\partial z}\left\{\rho D_i\left[\frac{\partial \chi_i}{\partial z} - \frac{\chi_i}{H}\left(1 - \frac{H}{H_i}\right)\right]\right\}, \quad (3)$$

where χ_i is the mixing ratio of species i; D_i is the molecular diffusion coefficient; $H_i = k_B T/(m_i g)$; k_B is Boltzmann's

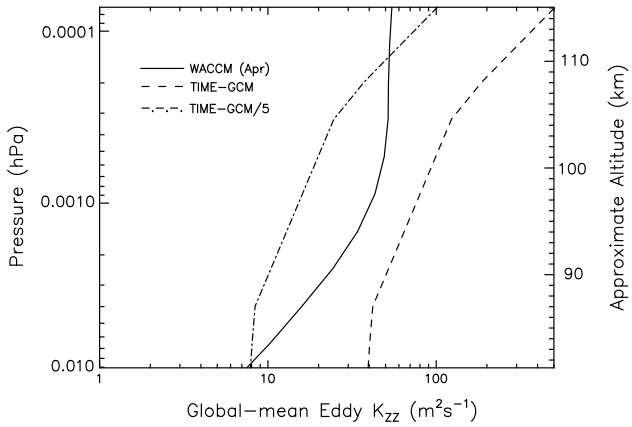

Figure 2. Vertical diffusion coefficient profiles calculated with WACCM (solid line) compared to the "standard" profile from TIME-GCM [*Roble*, 2000] (dashed line) and the same standard profile reduced by a factor of 5 (dash-dotted line). See text for details.

constant; T is the atmospheric temperature; m_i is the molecular weight of species i; g is the acceleration of gravity; $H = k_B T/(m_a g)$ is the atmospheric scale height; m_a is the mean molecular weight of air; and ρ is the atmospheric density. Equation (3) may be rewritten as

$$\frac{\partial \chi_i}{\partial t} = \frac{1}{\rho}\frac{\partial}{\partial z}\left(\rho D_i \frac{\partial \chi_i}{\partial z}\right) - \frac{1}{\rho}\frac{\partial(\rho w_i \chi_i)}{\partial z}, \quad (4)$$

where

$$w_i = \frac{D_i}{H}\left(1 - \frac{H}{H_i}\right) \quad (5)$$

is the "diffusive separation" velocity. The form (4) highlights the downgradient diffusion and differential advection aspects of molecular diffusion. The velocity w_i gives rise to diffusive separation because its value depends on the molecular weight of the minor species in question; w_i is negative for species heavier than the mean weight of air ($H_i < H$), such as CO_2, and positive for lighter species.

The calculation of eddy diffusion due to breaking gravity waves has changed with respect to earlier versions of WACCM, as noted above. Thus, it is important to document its behavior in the new model because, as shown by *López-Puertas et al*. [2000], too fast a rate of eddy diffusion can prevent realistic modeling of the vertical profile of CO_2 by counteracting the effect of molecular diffusive separation. Figure 2 shows the global-mean profile of the vertical eddy diffusion coefficient, K_{zz}, computed with the updated gravity wave parameterization in WACCM. This profile is compared with two other profiles discussed by López-Puertas et al., the "standard" K_{zz} used by *Roble* [2000] and the standard K_{zz} reduced by a factor of 5. Calculations using Roble et al.'s standard K_{zz} were not in good agreement with the CO_2 observations reviewed by López-Puertas et al. On the other hand, when the standard K_{zz} was reduced by a factor of 5, the calculations of CO_2 were in better agreement with observations. As shown in Figure 2, the values of K_{zz} calculated by WACCM are within a factor of 2 of the reduced K_{zz} profile considered by *López-Puertas et al*. in the critical altitude range 80–110 km, and somewhat smaller above 110 km.

It should also be borne in mind that the effective value of K_{zz} calculated with WACCM depends, among other things, on the value assumed for the Prandtl number, Pr, which describes the ratio of the eddy momentum flux to the eddy flux of chemical species [see *Garcia et al*., 2007]. The standard value used in the model is $Pr = 4$; we show below that the simulated vertical profile of CO_2 is sensitive to Pr and that comparison with observations suggests a lower value than adopted in the standard version of the model might be more appropriate.

3. Observations of CO_2 and CO

3.1. ACE CO_2 and CO

We use CO_2 and CO measurements taken by the Atmospheric Chemistry Experiment Fourier Transform Spectrometer (ACE-FTS) on SCISAT-1. These are solar occultation measurements, which, in contrast to observations derived from IR emissions, are not affected by non-local thermodynamic equilibrium (non-LTE) processes, particularly since only fundamental bands were used for the retrievals of CO_2 (above 65 km) and of CO [*Beagley et al*., 2010; *Clerbaux et al*., 2008]. The retrieval of CO_2 from ACE absorption spectra is described by *Boone et al*. [2005], and some additional details are given by *Beagley et al*. [2010]. CO_2 volume mixing ratio (vmr) in ACE is retrieved in the altitude range of 50 to 120 km. The vertical resolution is on average 3–4 km but varies from 2 to 6 km depending on the month, alternating from best to worst every other month, and being best during the months of February and April analyzed here. The random errors are altitude dependent and vary between about 2.5 and 5%. The total systematic errors run from 2% at the low altitudes (50–70 km) to about 5% at 90 km and increase at higher altitudes to 9% at 100 km and 16% at 118.5 km [*Beagley et al*., 2010].

CO vmr is retrieved from ACE absorption spectra in the range from 8 km to about 100 km. The retrieval method and an early validation of the (version 2.2) observations are described by *Clerbaux et al*. [2008]. As for CO_2, the retrieval is performed using occultation measurements from fundamental bands, (1–0) and (2–0), and hence are not affected by non-LTE processes. The vertical resolution in the altitude range studied here (above about 1 hPa) is about 4 km, but it can be as coarse as 6 km in the upper mesosphere. The noise errors of the ACE-FTS CO measurements are $< 5\%$ from the upper troposphere to 40 km and $< 10\%$ at higher altitudes. The derived systematic errors from the validation study are $< 15\%$ in the upper troposphere (8–12 km), $< 30\%$ in the lower stratosphere (12–30 km), and $< 25\%$ from 30 to 100 km.

For both CO_2 and CO, we used ACE data version 3.0. We discarded profiles known to have problems, as listed in https://databace.scisat.ca/validation/data_issues.php. Even after these data were eliminated, we found profiles with unphysical shapes, as well as some oscillating profiles, which were also discarded. A final filtering was carried out by removing profiles that differ from the annual mean by more than 5 standard deviations in any given year. In this study, we use the ACE (and MIPAS; see below) data for the months of February and April of 2007, 2008, and 2009. These 3 years are near the minimum in solar activity at the end of solar cycle 23 and the beginning of solar cycle 24; this obviates potential complications in interpretation due to changes in the rate of production of CO with changing solar activity, which can be large in the upper mesosphere and lower thermosphere [see, e.g., *Emmert et al*., 2012; *Lee et al*., 2013]. Both sunrise and sunset occultation observations were used. One disadvantage of occultation observations is that they have sparser temporal sampling and limited latitudinal coverage compared to emission measurements. To compensate for these problems, our comparisons with model results are based on monthly mean observations, which provide both a greater number of samples and more complete latitude coverage. The latitudes covered by ACE in 2007–2009 are 30°S to 80°N in February and 70°S to 80°S and 50°S to 45°N in April.

3.2. MIPAS CO

In addition to the ACE CO measurements, we also consider the global CO observations taken by the Michelson Interferometer for Passive Atmospheric Sounding (MIPAS). This was a limb emission Fourier transform spectrometer operating in the midinfrared spectral region [*Fischer et al*., 2008] onboard the Environmental Satellite (Envisat), which was launched in a Sun-synchronous polar orbit in March 2002 and operated continuously until 8 April 2012. For the period studied here, 2007–2009, MIPAS operated at the "optimized spectral resolution" (0.0625 cm^{-1}) [*Fischer et al*., 2008]. Most MIPAS measurements were taken in the standard observation, or "nominal," mode; however, this mode does not cover altitudes above about 70 km. Therefore, the measurements used here are those taken using the "middle atmosphere" mode (MA), which covers the altitude range 20–102 km with a vertical resolution of 3 km but with coarser resolution above that altitude. MIPAS was operated in this mode regularly but only on 1 day every 10 days. Hence, there are approximately 3 days of measurements per month for the period 2007–2009. We note that MIPAS MA measurements have a nominal uppermost tangent height of 102 km, while we use the retrieved CO up to 10^{-4} hPa (~ 115 km). The MIPAS MA observations of CO above 100 km have rather coarse vertical resolution, ~ 14 km, but similar accuracy as the observations below 100 km.

Vertical profiles of CO have been retrieved from the MIPAS spectra in the 4.7 μm region using a non-LTE retrieval scheme described in detail by *Funke et al*. [2009]. The vertical resolution of the retrieved CO profiles is 4–7 km below 60 km at night and below 95 km during daytime and larger than 7 km (up to 14 km) above those altitudes. The single-measurement precision (noise error) is 40–80% below 60 km and 30–60% above, depending mainly on latitude, with smaller values for polar winter conditions. The estimated systematic error ranges between 8 and 15% [*Funke et al*., 2009]. MIPAS nominal and MA CO data have been cross-validated with ACE-FTS observations [*Clerbaux et al*., 2008; *Hoffmann et al*., 2011]. Differences between the two instruments are typically within ±25%. MIPAS also agrees very well (within 10%) with ground-based microwave observations [*Forkman et al*., 2012].

3.3. Other Measurements

In addition to ACE and MIPAS, we also consider measurements of CO_2 and CO made by several other instruments: the Atmospheric Trace Molecule Spectroscopy experiment (ATMOS), the Improved Stratospheric and Mesospheric Sounder (ISAMS), and the Cryogenic Infrared Spectrometers and Telescopes for the Atmosphere instrument (CRISTA). Although these instruments did not provide extensive spatial and

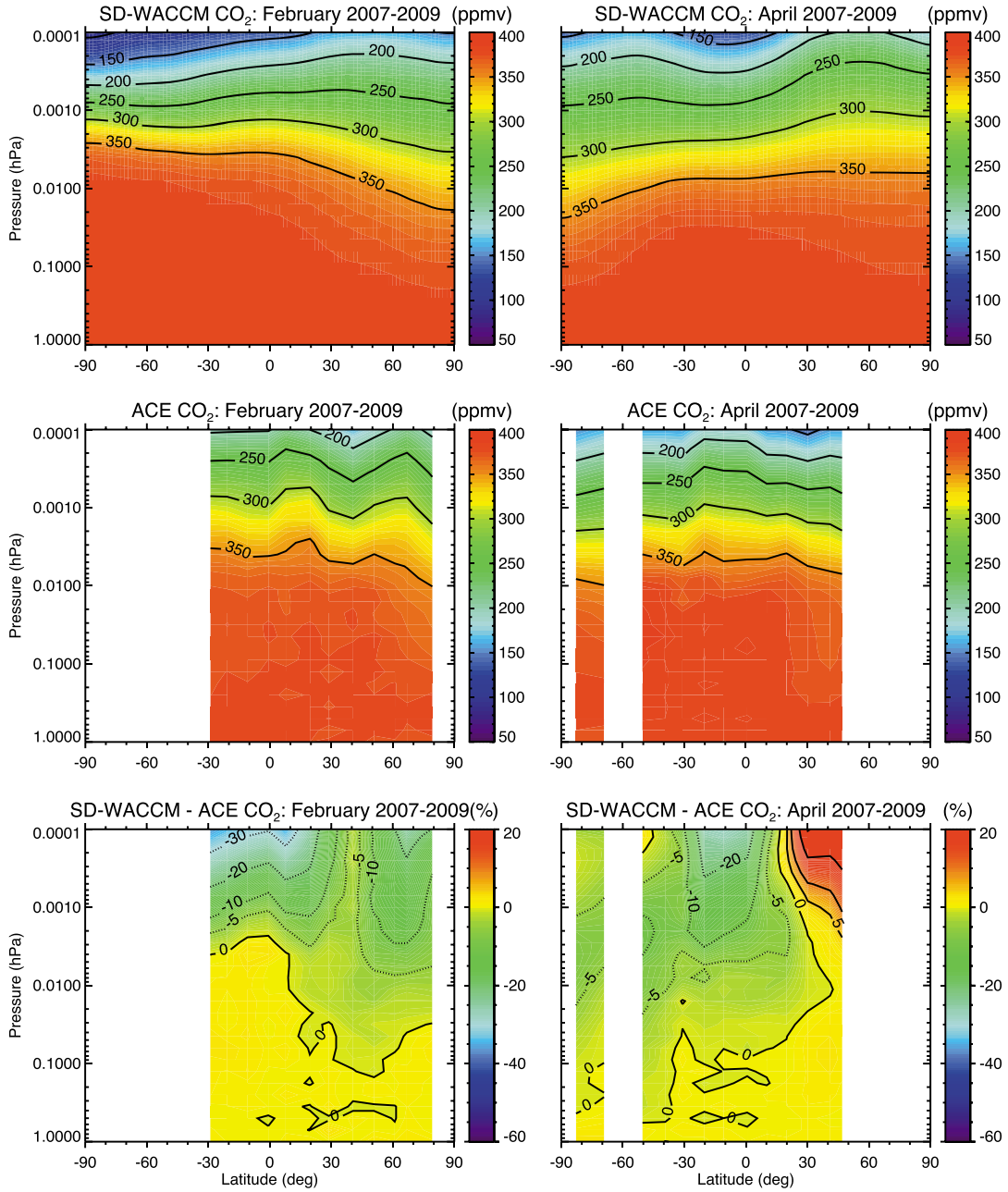

Figure 3. CO_2 mixing ratio (ppmv) calculated with WACCM (top row) and observed by ACE (middle row), and their percentage difference (bottom row), in February (left column) and April (right column). Model results and observations are averaged over 2007–2009.

temporal coverage, their observations of CO_2 and CO are important for confirming the general features of the vertical distribution of these gases. ATMOS flew on the Spacelab 3 shuttle mission and made occultation measurements of CO_2 and CO between 29 April and 6 May 1985. Six profiles were taken: four in the Northern Hemisphere between 26°N and 31°N and two in the Southern Hemisphere at 48.6°S and 46.4°S. More details on these measurements and their errors can be found in *López-Puertas et al.* [2000] and in *Rinsland et al.* [1992].

ISAMS flew onboard NASA's Upper Atmosphere Research Satellite and measured CO_2 globally from September 1991 through May 1992. These CO_2 measurements were retrieved from the daytime limb emission near 4.6 μm, which is produced by the non-LTE emission of CO_2. Note that, although the ISAMS profile discussed in

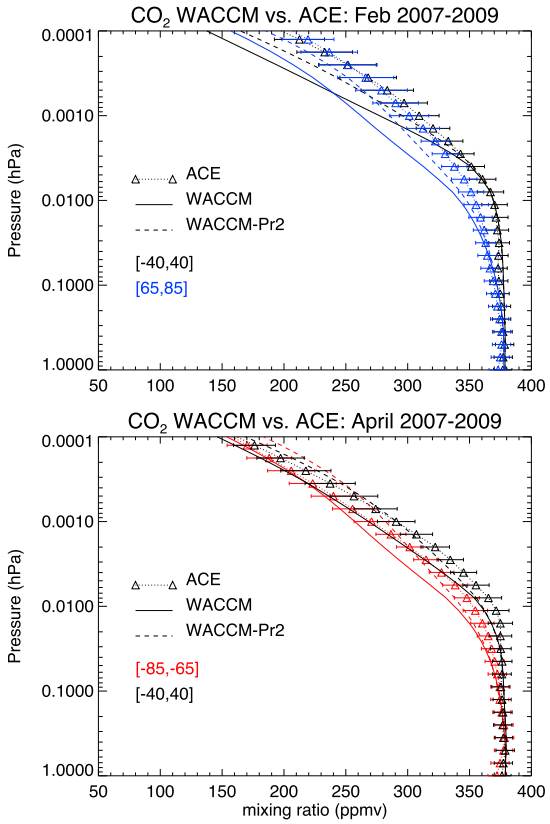

Figure 4. Vertical profiles of CO_2 mixing ratio in SD-WACCM (solid and dashed lines) and ACE (triangles) averaged over 40°S and 40°N and over 65–85°N and 65–85°S, for (top) February and (bottom) April. The error bars represent the 1 sigma systematic errors [from *Beagley et al*., 2010]; the instrumental errors of the averaged ACE data are negligible in comparison with the systematic errors. Model results and observations are also averaged over 3 years, 2007–2009. Two sets of calculations are shown for SD-WACCM: $Pr = 4$ (solid) and $Pr = 2$ (dashed). See text for details.

section 4 is a global mean, it can be considered as characteristic of midlatitudes because CO_2 was not retrieved at latitudes in polar night. More details on the ISAMS CO_2 measurements and their errors can be found in *Zaragoza et al*. [2000]. ISAMS also retrieved CO from infrared emissions using a non-LTE model. The ISAMS CO data discussed below correspond to the mean of the profiles taken in two 10° latitude bands centered at 30°N and 40°S on 1 April 1992. Note that, for this month, the latitudinal variation measured by ISAMS was very small [cf. *López-Puertas et al*., 2000, Figure 5b]. Additional details on the ISAMS data set are given by *López-Valverde et al*. [1996] and *López-Puertas et al*. [2000].

CRISTA flew onboard space shuttle mission STS-66 on 3–14 November 1994. CO_2 profiles are obtained from CRISTA measurements using the same non-LTE retrieval technique as used by ISAMS. That is, they are derived from the measured CO_2 4.3 μm non-LTE emission observed during illuminated conditions [*Kaufmann et al*., 2002]. The CRISTA-1 CO_2 profile discussed below corresponds to the global mean observed by CRISTA in November 1994 [see *Kaufmann et al*., 2002, Figures 3 and 14]. A global mean profile measured by CRISTA-2, on August 1997 (not shown), is very similar to that observed by CRISTA-1 [*Kaufmann et al*., 2002]. Since the data were all measured under illuminated conditions, the polar winter regions were not observed and are not included in the global mean profile.

4. Comparison of Modeled CO_2 and CO With Observations

4.1. Carbon Dioxide From ACE

Sampling of the MLT by ACE is not continuous because the solar occultation technique limits the time and location of the measurements. In order to enhance the statistical reliability of the observational results, we compare zonal-mean distributions of CO_2 as functions of latitude and altitude for the months of February and April, averaged over 3 years near solar minimum, 2007 to 2009. These months are representative of solstice and equinox conditions, respectively, and they happen to provide the broadest latitude coverage available from ACE. SD-WACCM zonal-mean CO_2 is available as monthly means of the instantaneously computed mixing ratio for all 3 years.

Figure 3 shows CO_2 mixing ratio distributions for February and April from ACE and SD-WACCM and the percentage differences with respect to ACE. There is good overall correspondence between model and observations in both months, and differences between the two are less than 10% below 10^{-3} hPa (about 100 km altitude). At higher levels, the differences are somewhat larger, generally between 10 and 20%; the largest discrepancies are found near 10^{-4} hPa (~115 km), the highest level where CO_2 is reliably observed by ACE. It is evident from this comparison that SD-WACCM is able to simulate the sharp falloff of CO_2 in the lower thermosphere observed by ACE; if anything, the calculated mixing ratio decreases too rapidly with altitude. These features can be appreciated more readily in the vertical profiles shown in Figure 4, which are latitude

means for the tropics and subtropics (40°S to 40°N) and for high latitudes (65–85°S or 65–85°N, depending on the ACE coverage available). CO_2 profiles simulated by SD-WACCM using the standard value of the Prandtl number in the gravity wave parameterization, $Pr = 4$, are denoted by the solid curves in Figure 4 (top and bottom). CO_2 begins to decrease around 0.01 hPa (~80 km) in both model and observations, but the rate of decrease is slightly faster in the model in certain seasons and latitude ranges. SD-WACCM CO_2 profiles mostly fall within the 1 sigma systematic error estimates of the ACE measurements in April for both latitude ranges considered, but the calculated CO_2 is significantly lower than observed by ACE in February, even at the 2 sigma level, at the highest altitudes.

Differences between SD-WACCM and ACE may be due in part to dynamical variability, particularly at high latitudes in winter. Even though the model is run with specified dynamics for the same years covered by the ACE measurements, the latter are not true monthly zonal means, as the occultation measurements are discontinuous in space and time. In addition, as noted earlier, the model is constrained by observations only below 1 hPa; above that altitude, SD-WACCM is free running, although its behavior is still conditioned by the state of the atmosphere at lower levels. However, in the 40°S–40°N results, the latitude averaging should remove advective transport effects due, for instance, to the mesopause semiannual oscillation (SAO). The fact that calculated CO_2 is still lower than observed by ACE in this case implies that the difference between model and observations might be due to vertical eddy mixing that is too weak in SD-WACCM.

Vertical eddy diffusion is calculated by the model's gravity wave parameterization, as described in *Garcia et al*. [2007] and *Richter et al*. [2010]. The magnitude of K_{zz} depends on several tunable parameters, such as the Prandtl number and the frequency with which the parameterized gravity wave spectrum is triggered by convection and frontogenesis. Adjustment of these parameters over a reasonable range would easily allow increases by a factor of 2–4 in the magnitude of K_{zz}. A simple test of the sensitivity of the model results to the magnitude of K_{zz} was carried out by reducing the Prandtl number, which increases the diffusion coefficient because, other things being equal, K_{zz} is inversely proportional to Pr. The dashed model profiles in Figure 4 show the result of setting $Pr = 2$. This change brings the model into agreement with observations within the estimated 1 sigma errors of the latter in almost all cases, although now the profiles for April show mixing ratios that are on the high side of the observations. This may be taken as evidence that the standard setting, $Pr = 4$, results in an underestimation of the value of K_{zz}; however, we emphasize that a reduction of Pr is not the only way in which the calculated diffusivity can be increased in the model, only the most straightforward one to implement. For example, changing the specification of the parameterized gravity wave spectrum that emanates from the troposphere (by altering the triggering due to convection or frontogenesis; see *Richter et al*. [2010]) can also change the magnitude and distribution of wave breaking and, hence, of K_{zz}.

As noted in section 1, *Beagley et al*. [2010] compared ACE data with calculations made with the Canadian Middle Atmosphere Model (CMAM). CMAM, like WACCM, is a "high-top" global model with fully interactive photochemistry and takes into account both eddy diffusion due to gravity waves and molecular diffusion. Nevertheless, Beagley et al. were able to match the ACE observations of CO_2 only when they artificially increased its rate of photolysis by a factor of 5, which, however, produced unrealistically large concentrations of CO. This result led Beagley et al. to conclude that there must exist a loss process for CO_2 that does not produce CO. They hypothesized that CO_2 might be sequestered in meteoritic dust via the mechanism proposed by *Plane* [2004]. Such a mechanism is clearly not necessary to simulate CO_2 successfully with SD-WACCM, but one might ask whether the model produces distributions of CO that are compatible with observations. We address this question next.

4.2. Carbon Monoxide From ACE and MIPAS

In the case of CO, data are available from both ACE and MIPAS, such that we can check for consistency between the two observational data sets, and between each data set and SD-WACCM calculations. As with CO_2, we compare monthly zonal means averaged over 2007–2009 with model results. Figure 5 shows CO mixing ratio distributions for February and April from ACE and SD-WACCM and the percentage differences relative to ACE. Note that, in the case of CO, ACE provides measurements up to 10^{-3} hPa only. As with CO_2, the main features of the observed distribution of CO are captured by the simulation, in particular the upward and downward tilt of the isolines of CO in the summer and winter hemispheres, respectively, in February and the flatter distribution in April. Nevertheless, there are some important local differences: In the

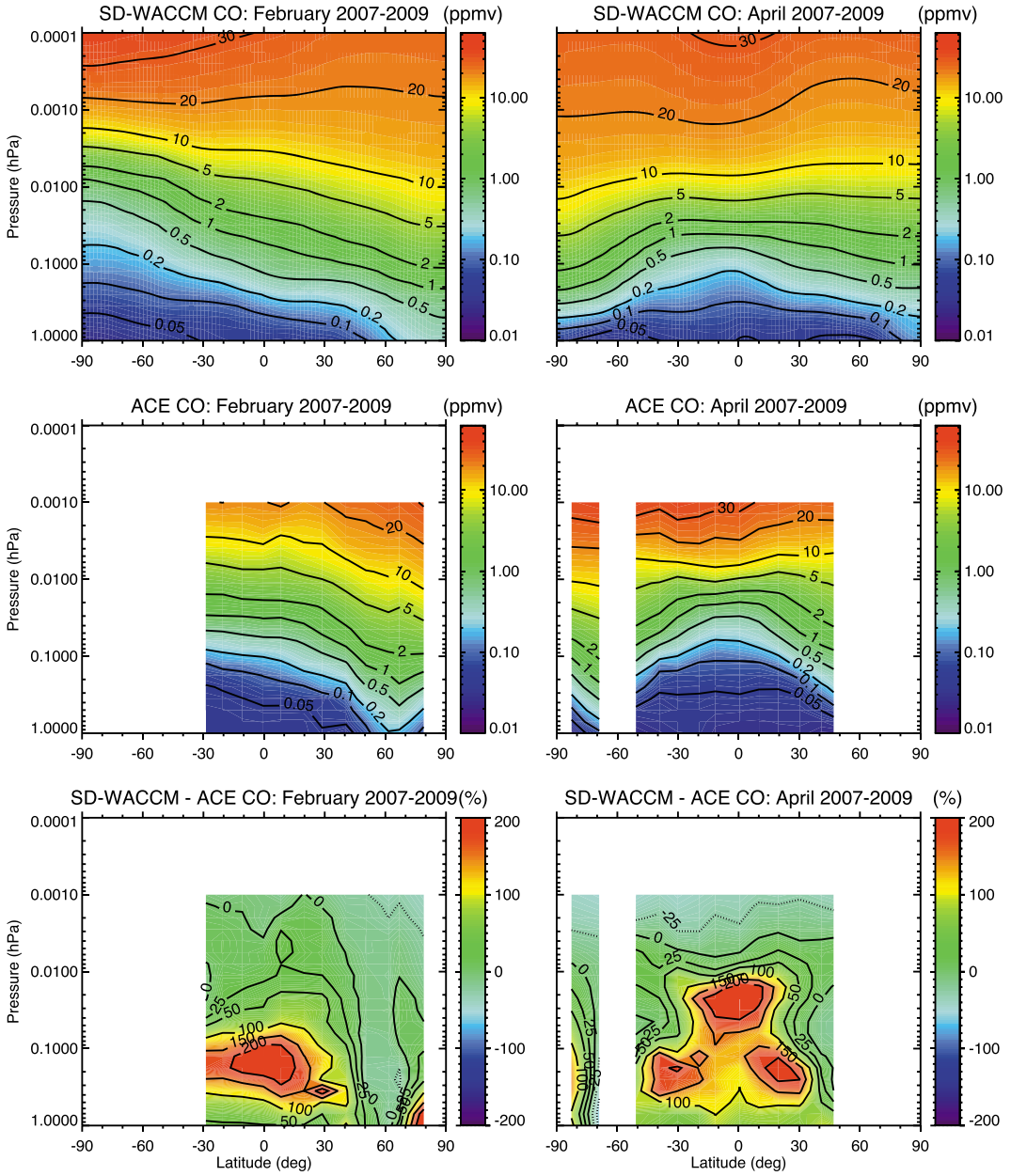

Figure 5. As in Figure 3 but for CO from SD-WACCM and ACE.

tropical and subtropical mesosphere, below about 0.01 hPa, SD-WACCM calculates up to twice more CO than is observed by ACE, whereas in the lower thermosphere the calculated CO is generally lower than observed by ACE. The large discrepancies below 0.01 hPa occur over a range of altitudes where the mixing ratio of CO is actually very small (less than 0.1 to a few ppmv), but the spatial coherence of the model-data differences and the fact that the 1 sigma systematic error of the measurements remains $< 25\%$ at these altitudes indicate that the differences are significant.

The surplus of calculated CO in the mesosphere is present in SD-WACCM results in both February and April; in February, it is confined to the lower mesosphere, below 0.1 hPa, while in April it extends throughout the mesosphere, to about 0.01 hPa. The pattern of CO differences between SD-WACCM and ACE has a distinctive latitudinal and vertical structure, which may be due to the effects of advection by the secondary meridional circulation associated with the mesospheric semiannual oscillation (SAO) [see, e.g., *Garcia et al.*, 1997].

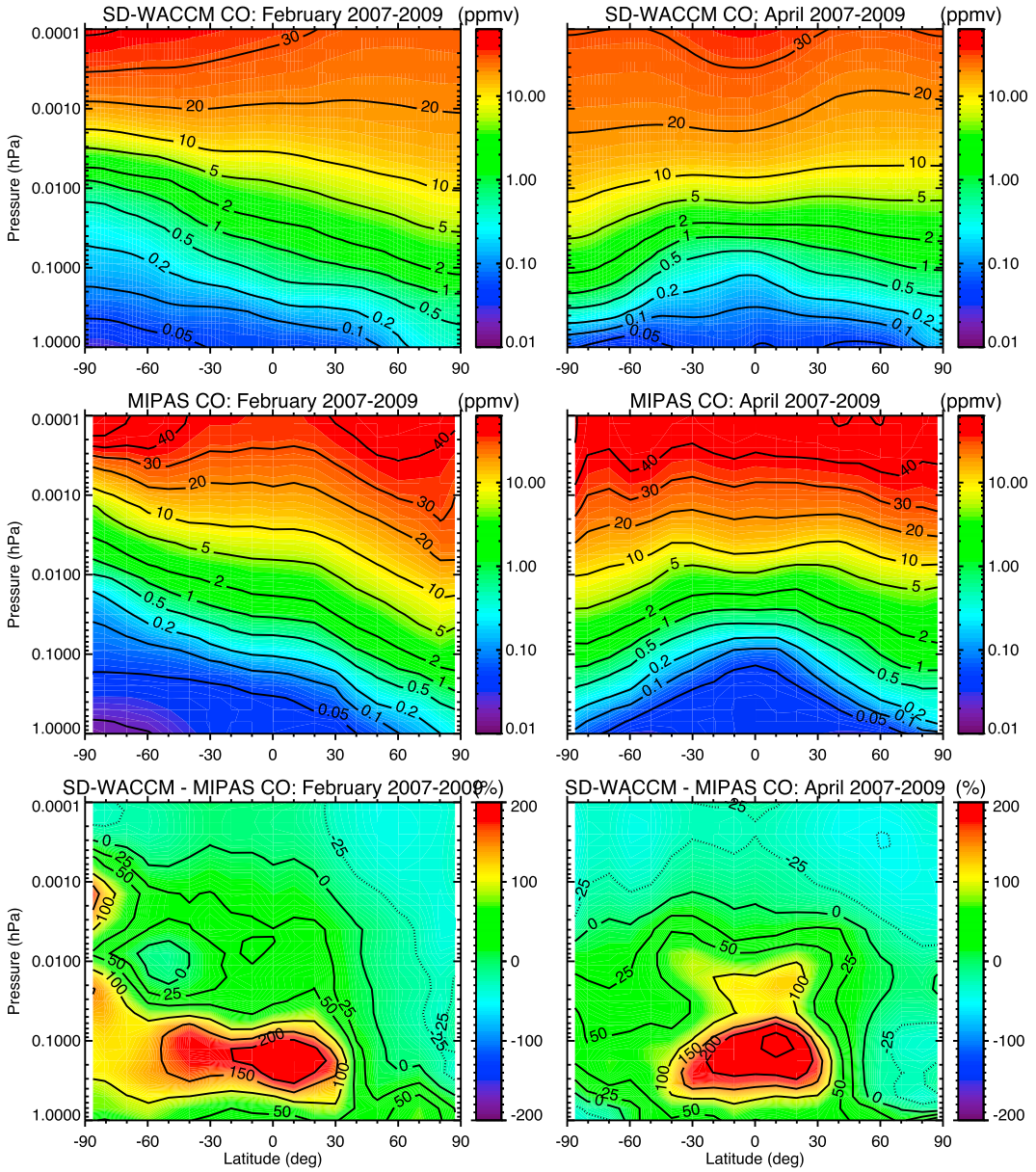

Figure 6. As in Figure 3 but for CO from SD-WACCM and MIPAS.

Comparison of SD-WACCM with MIPAS, Figure 6, reveals a similar pattern of differences between model and observations as seen with ACE; indeed, ACE and MIPAS measurements are highly consistent with each other, which suggests that the differences between the model and either set of observations are likely due to deficiencies in the model. In particular, CO in SD-WACCM is also higher than observed by MIPAS in the tropical and subtropical lower mesosphere in February, again by about a factor of 2, and the region of excess CO extends into the upper mesosphere in April. It is not clear why SD-WACCM produces considerably more CO in the tropical mesosphere than is observed by MIPAS and ACE; however, investigation of this problem is beyond the scope of the present study, which centers on the behavior of CO and CO_2 in the upper mesosphere and lower thermosphere.

Turning now to the simulation of CO in the upper mesosphere and lower thermosphere, above ~ 0.01 hPa, we note that CO calculated with SD-WACCM is lower than observed by ACE by up to 25%. This deficit extends into the lower mesosphere in northern high latitudes in February. MIPAS observations of CO (Figure 6), which

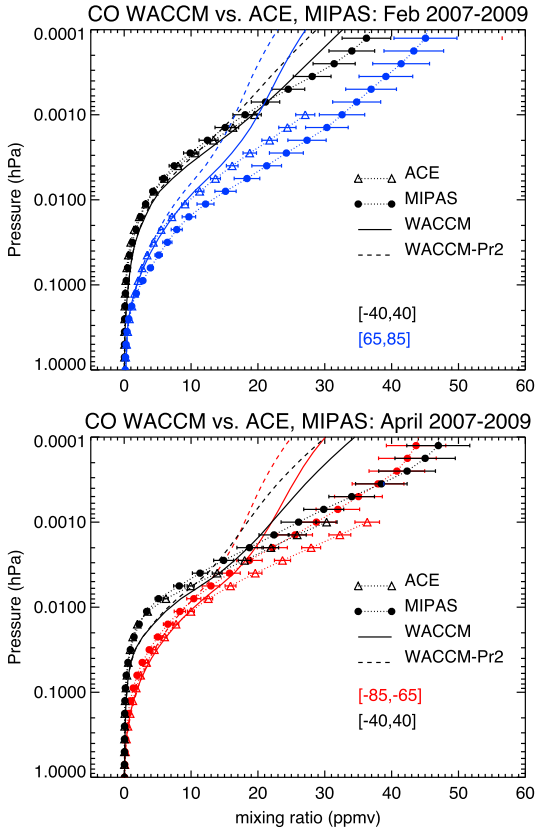

Figure 7. As in Figure 4 but for CO from SD-WACCM, ACE, and MIPAS. ACE and MIPAS data are denoted by triangles and filled circles, respectively. One sigma systematic errors are shown for both ACE and MIPAS.

reach 10^{-4} hPa (~115 km), confirm the model deficit in CO seen in the comparison against ACE and show that it increases in the altitude range 10^{-3} to 10^{-4} hPa (~100–115 km). Near 10^{-4} hPa, CO calculated with SD-WACCM is almost 50% lower than observed by MIPAS at some locations. At high latitudes of the Northern Hemisphere, the model CO deficit against MIPAS also extends into the lower mesosphere in February, and a region of low CO with respect to MIPAS persists below 0.1 hPa even in April. These patterns are much more evident in MIPAS than in ACE observations due to the continuous high latitude coverage of the latter, and they appear to be consistent with transport, by the downwelling circulation of northern winter, of model CO deficits that originate in the lower thermosphere.

Figure 7 compares latitude-average profiles of CO from SD-WACCM, ACE, and MIPAS in the tropics and subtropics (40°S–40°N), and northern and southern high latitudes (65–85°N and S). The model and observational profiles are plotted using a linear scale for the mixing ratio, as opposed to the logarithmic scale used in the contour plots shown in Figures 5 and 6. This is done to emphasize the behavior in the upper mesosphere and lower thermosphere, which is the focus of this study. The profiles of Figure 7 confirm the consistency of the model-measurement differences in both observational data sets at essentially all latitudes and seasons and show that SD-WACCM calculates too little CO in the lower thermosphere compared to that of observations, especially between 10^{-3} and 10^{-4} hPa (about 100–115 km). Note, by the way, that the simulation with decreased Prandtl number, $Pr = 2$, which tended to improve the agreement with observations in the case of CO_2, actually degrades the agreement for CO (dashed profiles in Figure 7), as the stronger vertical diffusion that results from this change increases the downward flux of CO (and leads to a larger negative flux divergence in the lower thermosphere). The model deficit in CO in the lower thermosphere is interesting because it demonstrates that the rate of decrease of CO_2 with altitude documented in the previous section does not imply a corresponding rate of increase of CO. It also raises the question, which we take up in section 5, why the observations show considerably more CO in this region than the model calculates even though CO_2 agrees well with observations.

4.3. Other Observations

The ACE and MIPAS data sets together provide global or near-global observations of CO_2 and CO throughout the mesosphere and lower thermosphere over several years. Observations of these gases are also available from three additional satellite instruments: ATMOS, CRISTA, and ISAMS, described in section 3.3. Although these observations are more restricted in their spatial and temporal coverage, it is still of interest to determine whether the differences found in the comparisons between SD-WACCM and the ACE and MIPAS data sets are also present in comparisons against other data.

Figure 8a shows vertical profiles of CO_2 simulated with SD-WACCM against ATMOS, CRISTA, and ISAMS observations. Data from ACE are also included to illustrate the consistency between this data set and the other observations. The profiles are shown as functions of geometric altitude, which is the native vertical coordinate system of the ATMOS, CRISTA, ISAMS, and ACE measurements. SD-WACCM results, which are registered in pressure, are converted to geometric height coordinates using the height versus pressure

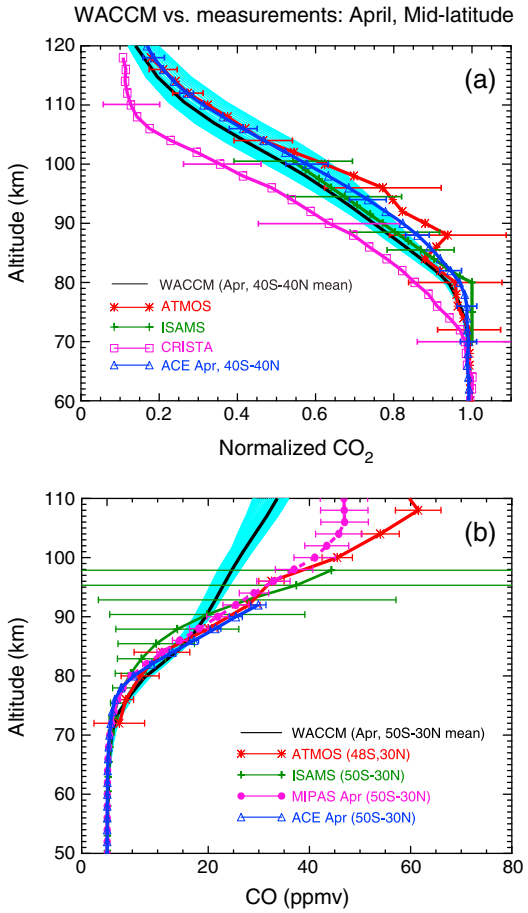

Figure 8. Comparison of (a) CO_2 and (b) CO profiles calculated SD-WACCM using $Pr = 4$ with results from several data sets (symbols, with 1 sigma systematic error bars). Model profiles are shown as blue solid lines for latitudes in the range 40°S–40°N for CO_2 and 50°S–30°N for CO. The black solid lines denote the mean of all model profiles in each latitude range. For CO_2, the abscissa is normalized to the mixing ratio at 60 km. Note different vertical ranges.

relationship from ACE [*Beagley et al*., 2010]. The data are shown normalized with respect to the mixing ratio of CO_2 at 60 km to account for the anthropogenic increase of CO_2 in the well-mixed atmosphere over the time span of the measurements. The comparison indicates that with the exception of CRISTA, the calculated CO_2 profiles are on the low side of the observations, although mostly within their 1 sigma error bars. CRISTA, on the other hand, observes significantly lower values of CO_2 than the model results (and the rest of the observations). Disregarding the CRISTA measurements, it may be concluded that the vertical profile of CO_2 at tropical and middle latitudes is consistently observed by all instruments and that WACCM is able to simulate this profile, albeit with somewhat smaller mixing ratio overall. As noted above, this may be taken to imply that the vertical diffusion coefficient calculated by the gravity wave parameterization underestimates somewhat the rate of mixing in the real atmosphere.

Figure 8b compares profiles of CO calculated with SD-WACCM against observations by ATMOS, ISAMS, MIPAS, and ACE. The CO observations are mostly mutually consistent in the lower thermosphere, and they all indicate higher mixing ratios than modeled with WACCM. The deficit of modeled CO in the thermosphere, which increases with altitude, remains the most important discrepancy in the WACCM simulations of CO and CO_2. We address this question in the following section.

5. Discussion and Conclusions

SD-WACCM results are generally in good agreement with the global, multiyear ACE CO_2 observations, as well as with occasional measurements made by ATMOS and ISAMS. However, the standard version of the model tends to underestimate slightly the mixing ratio of CO_2 compared to the ensemble of these observations at levels above 10^{-3} hPa, as shown, for example, in Figure 4. The sensitivity of the calculated profile to the vertical diffusion coefficient, K_{zz}, was evaluated above by halving the Prandtl number used in the calculation of K_{zz}, which has the effect of roughly doubling the value of the diffusion coefficient. Such a change improves the agreement between calculations and observations in most locations and seasons and suggests (but does not conclusively prove—see below) that the standard setting used for the Prandtl number, $Pr = 4$, might lead to an underestimate of K_{zz}.

In any case, it is clear that, contrary to the conclusions of *Beagley et al*. [2010], there is no need in the present calculations to invoke any additional loss mechanism to explain the rapid decrease of CO_2 with altitude in the lower thermosphere. Furthermore, low values of CO_2 in the thermosphere do not lead to unrealistically large abundances of CO because, in SD-WACCM, the mean CO_2 profile below 10^{-4} hPa (~ 115 km) is determined principally by the balance between diffusive separation and eddy diffusion, with photolysis playing a minor role. This can be illustrated explicitly by comparing the characteristic global lifetimes of CO_2 against photolysis, eddy diffusion, downgradient molecular diffusion, and diffusive separation, which are the principal terms in the globally averaged budget of CO_2 in SD-WACCM. These lifetimes are estimated by

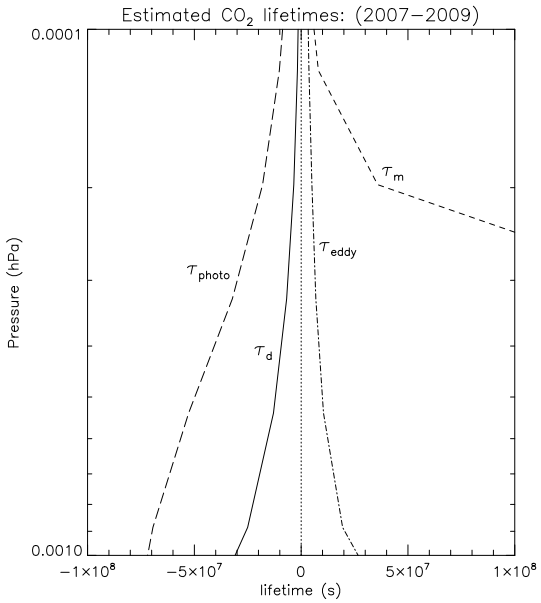

Figure 9. Global-mean lifetimes of CO_2 with respect to various transport and loss processes averaged over the period 2007–2009: diffusive separation, τ_d; molecular diffusion, τ_m; eddy diffusion, τ_{eddy}; and photolysis, τ_{photo}. The sign denotes whether the various processes act to reduce or increase CO_2. See text for details.

dividing the globally averaged abundance of CO_2 by the globally averaged tendency due to each process as functions of altitude. Thus, the diffusive separation lifetime is defined as

$$\tau_d(z) = \frac{\langle CO_2(z)\rangle}{\left\langle -w_d \frac{\partial CO_2(z)}{\partial z}\right\rangle}, \quad (6)$$

where w_d is the diffusive separation velocity (5) and the brackets denote global averaging. Similarly, the lifetime due to eddy diffusion is calculated as

$$\tau_{eddy}(z) = \frac{\langle CO_2(z)\rangle}{\left\langle \frac{1}{\rho}\frac{\partial}{\partial z}\left(\rho K_{zz}\frac{\partial CO_2(z)}{\partial z}\right)\right\rangle}, \quad (7)$$

and so on for the other transport and loss processes. The sign of the different lifetimes may be positive or negative, depending on whether the process in question tends to reduce or increase the abundance of CO_2.

Figure 9 shows these lifetimes in the pressure range 10^{-3} to 10^{-4} hPa (~ 100–115 km); it can be seen that the fastest processes by far are diffusive separation, denoted by τ_d, which tends to reduce CO_2, and eddy diffusion, τ_{eddy}, which tends to increase it. Downgradient molecular diffusion and photolytic loss are much slower throughout most of the range shown, although downgradient molecular diffusion becomes more important near 10^{-4} hPa. Because the equilibrium CO_2 profile in the range 10^{-3} to 10^{-4} hPa is determined mainly by the competition between diffusive separation and eddy diffusion, and not by photolytic or chemical loss, the rapid falloff of CO_2 with altitude in this region does not imply a correspondingly large increase in CO.

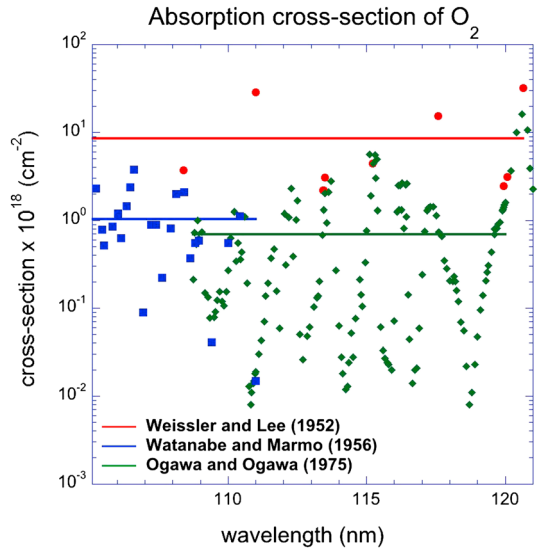

Figure 10. Experimental determinations of the absorption cross section of O_2 in the 105–121 nm wavelength range. The solid horizontal lines denote the mean value over the wavelength interval of each set of measurements. The value used in the standard version of WACCM is comparable to the average of the results of *Weissler and Lee* [1952], which in turn is nearly 10 times larger than the other measurements shown. See text for details.

In fact, SD-WACCM underestimates the mixing ratio of CO in the lower thermosphere with respect to all available observations (cf. Figures 7 and 8b), and this constitutes the most important deficiency of our standard simulation in the MLT. Insight into the cause of the problem may be gained by examining the seasonal cycle of CO in the model against MIPAS observations, which cover the period 2007–2009 continuously, from the stratopause to the lower thermosphere. Comparison of the observed and calculated seasonal variation of CO (not shown) indicates that the model reproduces well the seasonal cycle except in the lower mesosphere (~0.1 hPa and below), where CO is overestimated, as discussed above in connection with Figures 5 and 6. However, the calculated CO mixing ratio in the lower thermosphere, above 10^{-3} hPa, is uniformly lower than observed throughout the year in all latitude ranges considered. This suggests a deficit in the calculated production of CO at those altitudes.

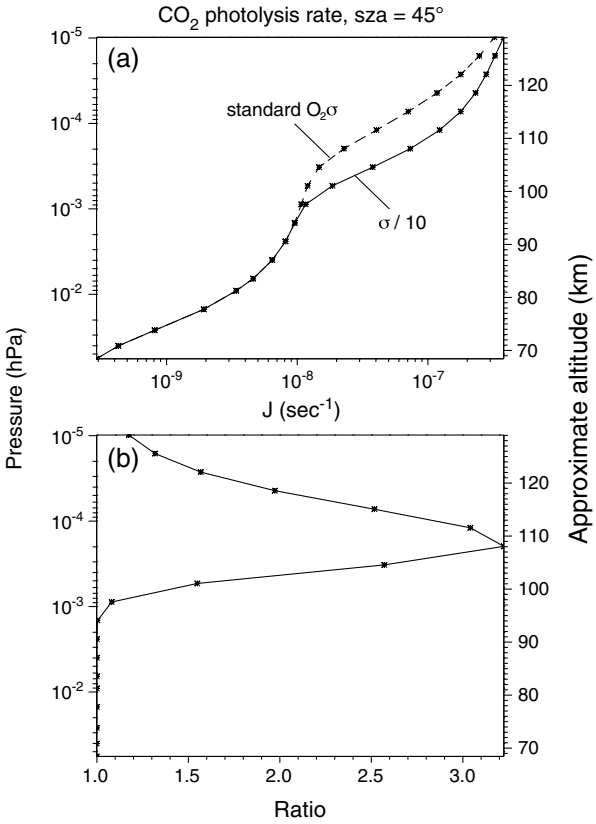

Figure 11. (a) Comparison of the total photolysis rate of carbon dioxide calculated with the standard version of WACCM, which uses a large absorption cross section for O_2 in the wavelength interval 105–121 nm, $\sigma = 5.8 \times 10^{-18}$ cm^{-2}, and the photolysis rate calculated when σ is reduced by a factor of 10. (b) Ratio of the photolysis rates for the runs with reduced versus standard σ. See text for details.

The production rate of CO above 10^{-3} hPa could be underestimated in SD-WACCM for a number of reasons, of which the most plausible are uncertainties in the rate of reaction, k, of CO_2 with O^+, and inaccuracies in the calculation of CO_2 photolysis at EUV wavelengths < 121 nm, J_{EUV}. These sources of CO were identified and included in SD-WACCM during the present investigation, as discussed in section 2. As regards k, *Fox and Sung* [2001] quote a value of 1.1×10^{-9} cm^3 s^{-1} for temperatures < 800 K. Values between 9×10^{-10} and 1.2×10^{-9} cm^3 s^{-1} are quoted by *Hunton et al*. [1991], with a "currently accepted" value of 9.4×10^{-10} cm^3 s^{-1}. The standard version of WACCM uses $k = 9 \times 10^{-10}$ cm^3 s^{-1}, which is at the low end of this range. A calculation (not shown) where the rate of reaction of CO_2 with O^+ was set to 1.2×10^{-9} cm^3 s^{-1} yielded an increase of about 15% (5 ppmv) in the mixing ratio of CO near 10^{-4} hPa, which is not nearly enough to make up the 10–20 ppmv deficit in calculated CO with respect to observations seen in Figures 7 and 8b. This is not surprising, because the reaction $CO_2 + O^+$ is the dominant source of CO only above ~ 120 km.

On the other hand, photolysis at EUV wavelengths is important in the altitude range 100–120 km (see Figure 1), where SD-WACCM underestimates CO relative to observations. Calculation of J_{EUV} could be inaccurate because both the solar irradiance and the cross section of CO_2 are highly structured functions of wavelength between 90 and 121 nm; indeed, both can vary by an order of magnitude over a range of 1 nm, or even smaller. SD-WACCM uses coarse bins for EUV radiance and CO_2 cross section at wavelengths < 121 nm, and the size of these bins ranges from a few nanometers to as much as 16 nm. To investigate the impact of spectral resolution on the production rate of CO, we used the photolysis model developed at the Instituto de Astrofísica de Andalucía (IAA) [*González-Galindo et al*., 2005] to compute CO_2 photolysis at low and high spectral resolution in the range 90–121 nm. The low-resolution calculations used the same wavelength bins as SD-WACCM, while the high-resolution calculations were made using 0.1 nm intervals. The results (not shown) confirm that, at altitudes below 100 km, the use of coarse spectral intervals does result in a large underestimate of the photolysis rate at 90–121 nm. Nevertheless, this has an insignificant effect on the production rate of CO because, at those altitudes, production is dominated by photolysis of CO_2 at longer (UV) wavelengths (Figure 1).

However, further comparison of SD-WACCM and the IAA model revealed that the standard version of SD-WACCM uses a very large cross section for molecular oxygen, O_2, in the wavelength bin 105–121 nm, $\sigma_{O2} = 5.8 \times 10^{-18}$ cm^{-2}. This value is comparable to the average of the measurements of *Weissler and Lee* [1952] but much larger than the results of two other experimental determinations, by *Ogawa and Ogawa* [1975] and *Watanabe and Marmo* [1956], which indicate values about 10 times smaller, as shown in Figure 10. Therefore, we tested the sensitivity of the photolysis rate of CO_2 to a tenfold reduction of the O_2 cross section used by SD-WACCM in the 105–121 nm bin. We found substantial increases in the total rate of photolysis between about 95 and 115 km (10^{-3} to 10^{-4} hPa), peaking near 105 km, as illustrated in Figure 11. This is

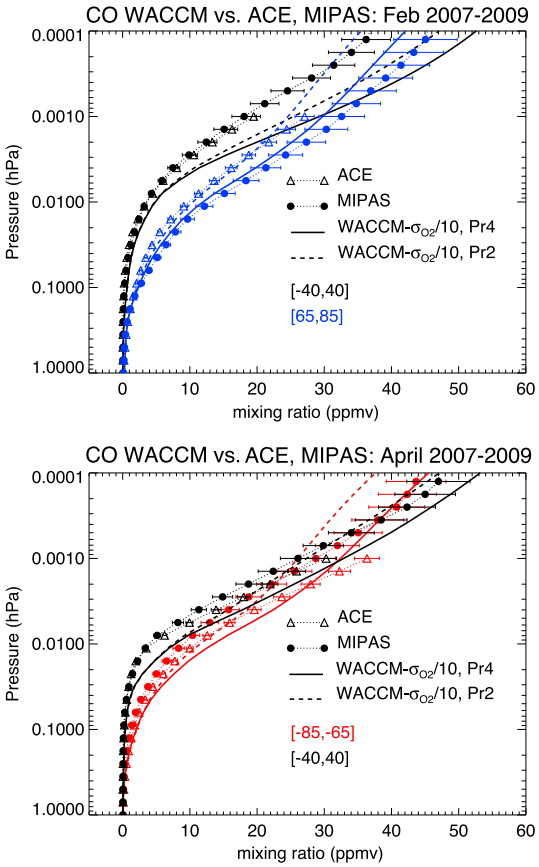

Figure 12. As in Figure 7 but for a calculation when the absorption cross section of O_2 is set to 0.58×10^{-18} cm^{-2} in the wavelength range 105–121 nm. Results for two different values of the Prandtl number, *Pr*, are shown. Model results using $Pr = 4$ are denoted by the solid curves and those with $Pr = 2$ by the dashed curves.

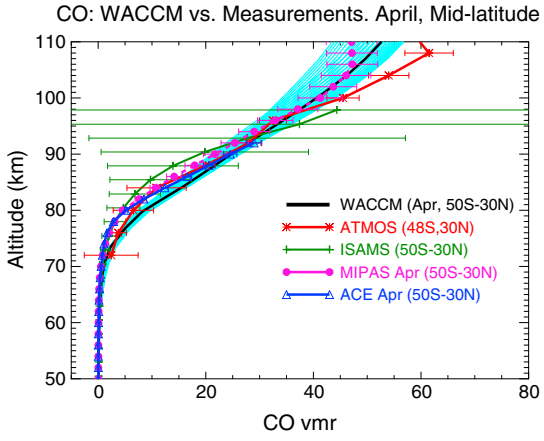

Figure 13. As in Figure 8b but for a calculation using the value 0.58×10^{-18} cm^{-2} for the cross section of O_2 of in the wavelength range 105–121 nm and $Pr = 2$.

precisely the range of altitude where SD-WACCM underpredicts the abundance of CO. Evidently, the large O_2 cross section used in the standard version of the model extinguishes much of the EUV flux in the range 105–121 nm at high altitudes, whereas the smaller cross section allows a much greater fraction of this flux to penetrate below 115 km. Additional calculations made with the IAA model at high spectral resolution (not shown) yield similar results, indicating that the crucial factor for computing CO_2 photolysis in the EUV is the magnitude of σ_{O2} and not the spectral resolution. The largest enhancement in the photolysis is about a factor of 3 (Figure 11b) in both cases, although the details are influenced by the spectral resolution. In particular, the enhancement in the high-resolution calculation peaks at about 3 km lower altitude.

Figure 12 shows a comparison against ACE and MIPAS observations of CO profiles from two simulations in which a reduced O_2 cross section, $\sigma_{O2} = 0.58 \times 10^{-18}$ cm^{-2}, was used with different values of the Prandtl number, $Pr = 2$ and $Pr = 4$. The results now reproduce much more closely the large CO mixing ratios, in the range 35–50 ppmv, observed above 10^{-3} hPa (cf. Figures 7 and 12). We note that no single value of *Pr* yields the best agreement in all instances; at higher latitudes, the observations are matched best by the calculations that use the standard model value, $Pr = 4$, but at lower latitudes $Pr = 2$ leads to better agreement. Midlatitude observations, Figure 13, are also matched closely with $Pr = 2$. All of this suggests that deficiencies in the modeling of eddy diffusive transport may be due to problems in producing the correct latitudinal variation of K_{zz} and cannot be addressed simply by adjusting the Prandtl number. Alternatively, calculations made at higher spectral resolution might produce (zenith angle-dependent) latitudinal variations in CO_2 photolysis that could improve the agreement between model and observations. Investigation of these matters, as well as any attempt to ascertain more accurately the Prandtl number for eddy diffusion, is beyond the scope of the present study. Be that as it may, we compare in Figure 14 the seasonal cycle of CO in MIPAS and SD-WACCM, using the reduced O_2 cross section at 105–121 nm and $Pr = 2$ to show that, with these parameter settings, the model reproduces remarkably well most details of the observed seasonal cycle in the MLT apart from the deficiencies already noted.

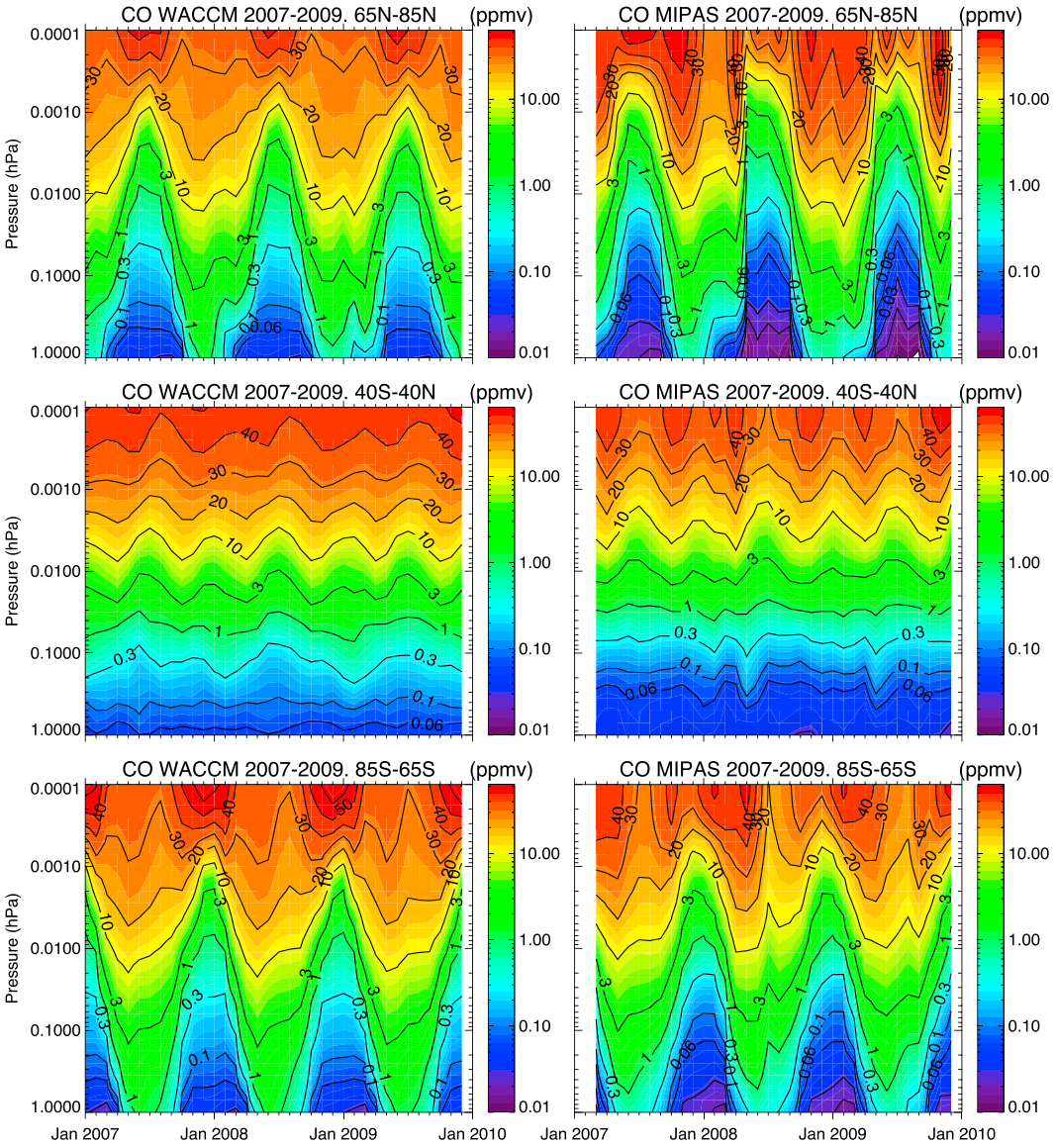

Figure 14. Seasonal cycle of CO in three ranges of latitude observed by MIPAS (right column) and calculated with SD-WACCM (left column) with a reduced absorption cross section for O_2 (0.58×10^{-18} cm^{-2}) at 105–121 nm and $Pr=2$.

Finally, as may be inferred from the discussion of Figure 10 above, the faster photolysis rate of CO_2 that results from reducing σ_{O2} by a factor of 10 at 105–121 nm produces relatively minor changes in the vertical profile of this species. For example, in the latitude range ±40° in April (Figure 4), the mixing ratio of CO_2 at 10^{-4} hPa is 150 ppmv in the standard calculation ($\sigma_{O2}=5.8\times10^{-18}$ cm^{-2} and $Pr=4$), while ACE observations show a value of ~170 ± 20 ppmv; the calculated mixing ratio drops to about 140 ppmv when a reduced cross section, $\sigma_{O2}=0.58\times10^{-18}$ cm^{-2}, is adopted without changing Pr. When $Pr=2$ is used, the corresponding values are 170 and 160 ppmv for calculations with the large and small values of σ_{O2}, respectively.

This study has emphasized detailed comparisons of zonal-mean, monthly mean results between WACCM and the ACE and MIPAS data sets. As discussed earlier, this has been done because we wished to enhance the statistical reliability of the observations, which are sparse in time for both instruments, and also in space in the case of the ACE occultation measurements. Furthermore, insofar as model output is not available at the precise space and time coordinates of the observations, the use of zonal

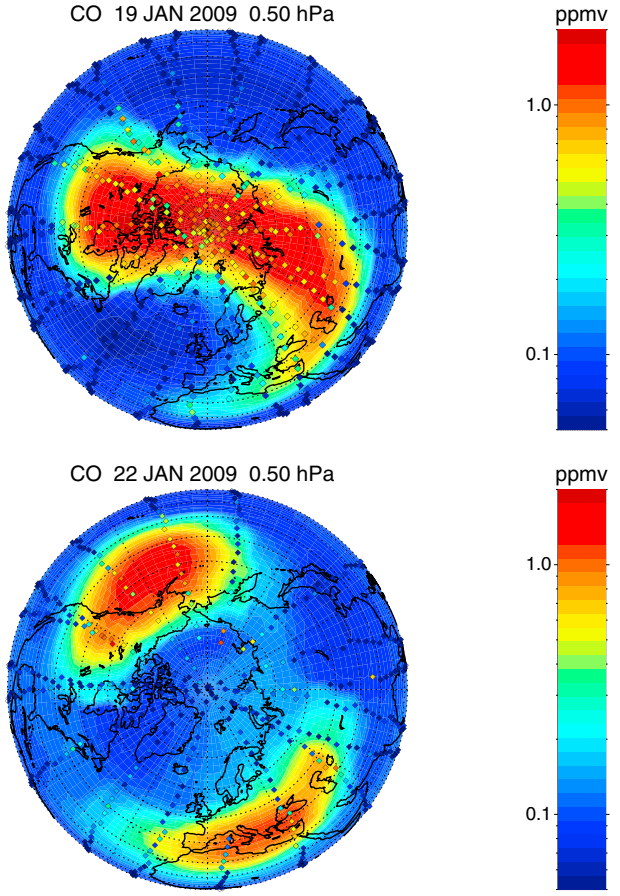

Figure 15. Distribution of CO on the 0.5 hPa pressure surface simulated by WACCM (filled contours) and observed by MIPAS (diamonds) on two dates, (top) before and (bottom) during the major stratospheric sudden warming of January 2009.

and monthly means helps alleviate potential tidal aliases at altitudes above ~90 km, where the effect of the tides becomes large. Model results are, of course, fully three-dimensional, and one might ask whether they capture the influence of dynamics, in particular during times when the atmosphere is strongly disturbed by large-scale waves. Figure 15 shows a comparison of CO calculated by WACCM and observed by MIPAS at 0.5 hPa on 19 and 22 January 2009, before and during a major stratospheric sudden warming (SSW) [see, e.g., *Harada et al*., 2010]. Before the SSW (Figure 15, top), the latitudinal distribution of CO has the expected wintertime structure, with large mixing ratios over the polar cap due to downwelling of CO-rich air from higher altitudes. After the onset of the SSW (Figure 15, bottom), the latitudinal distribution of CO is reversed and shows low mixing ratios over the polar cap and a pair of high-mixing ratio regions in midlatitudes, which correspond to the remnants of the split polar vortex. This pattern is clearly captured by both the simulation and the observations, although the absolute mixing ratios do not always coincide.

In summary, the results presented here suggest that there are no major deficiencies in our current understanding of the photochemistry of CO and CO_2 in the MLT, such that the observed variability of these species and, in particular, the shape and magnitude of their vertical profiles can, for the most part, be simulated accurately. Our calculations do indicate that inclusion of CO production from the reaction of O^+ with CO_2, and especially from photolysis of CO_2 at EUV wavelengths < 121 nm, is needed to produce the large mixing ratios of CO observed above 10^{-3} hPa (~ 100 km) and that the calculation of EUV photolysis requires adoption of an absorption cross section for O_2 at 105–121 nm no larger, on average, than about 10^{-18} cm^{-2}.

Acknowledgments
We thank Kaley Walker for helping us access the ACE data and advising us on its use; Jean-François Lamarque, Sasha Madronich, and Stan Solomon for their comments on the original version of the paper; and Simon Chabrillat and an anonymous reviewer for additional comments and suggestions that have improved substantially the final version. The National Center for Atmospheric Research (NCAR) is sponsored by the U.S. National Science Foundation. R.R. Garcia was supported in part by NASA grant X09AJ83G. M. López-Puertas and B. Funke were supported by MINECO (Spain) under grant AYA2011-23552, the CONSOLIDER program CSD2009-00038, and EC FEDER funds. F. González-Galindo was supported by a JAE-doc contract from CSIC (Spain), cofinanced by the European Social Fund. WACCM is a component of the Community Earth System Model (CESM), which is supported by the National Science Foundation (NSF) and the Office of Science of the U.S. Department of Energy. Computing resources were provided by NCAR's Climate Simulation Laboratory, sponsored by NSF and other agencies. This research was enabled by the computational and storage resources of NCAR's Computational and Information Systems Laboratory (CISL).

References

Banks, P. M., and G. Kockarts (1973), *Aeronomy*, Part B, 355 pp., Academic Press, New York.
Beagley, S. R., C. D. Boone, V. I. Fomichev, J. J. Jin, K. Semeniuk, J. C. McConnell, and P. F. Bernath (2010), First multi-year occultation observations of CO_2 in the MLT by ACE satellite: Observations and analysis using the extended CMAM, *Atmos. Chem. Phys.*, *9*, 1133–1153.
Boone, C. D., R. Nassar, K. A. Walker, and Y. Rochon (2005), Retrievals for the atmospheric chemistry experiment Fourier-transform spectrometer, *Appl. Opt.*, *44*(33), 7218–7231.
Chabrillat, S., G. Kockarts, D. Fonteyn, and G. Brasseur (2002), Impact of molecular diffusion on the CO_2 distribution and temperature in the mesosphere, *Geophys. Res. Lett.*, *29*(15), 1729, doi:10.1029/2002GL015309.
Clerbaux, C., et al. (2008), CO measurements from the ACE-FTS satellite instrument: Data analysis and validation using ground-based, airborne and spaceborne observations, *Atmos. Chem. Phys.*, *8*, 2569–2594.
Emmert, J. T., M. H. Stephens, P. F. Bernath, D. P. Drob, and C. D. Boone (2012), Observations of increasing carbon dioxide concentrations in the Earth's thermosphere, *Nat. Geosci.*, *5*, 868–871, doi:10.1038/ngeo1626.
Fischer, H., et al. (2008), MIPAS: An instrument for atmospheric and climate research, *Atmos. Chem. Phys.*, *8*, 2151–2188.
Forkman, P., O. M. Christensen, P. Eriksson, J. Urban, and B. Funke (2012), Six years of mesospheric CO estimated from ground-based frequency-switched microwave radiometry at 57°N compared with satellite instruments, *Atmos. Meas. Tech.*, *5*, 2827–2841, doi:10.5194/amt-5-2827-2012.
Fox, J. L., and A. Dalgarno (1979), Ionization, luminosity, and heating of the upper atmosphere of Mars, *J. Geophys. Res.*, *84*, 7315–7333.
Fox, J. L., and K. Y. Sung (2001), Solar activity variations of the Venus thermosphere/ionosphere, *J. Geophys. Res.*, *106*, 21,305–21,335.
Funke, B., et al. (2009), Carbon monoxide distributions from the upper troposphere to the mesosphere inferred from 4.7μm non-local thermal equilibrium emissions measured by MIPAS on ENVISAT, *Atmos. Chem. Phys.*, *9*(7), 2387–2411.
Garcia, R. R., T. J. Dunkerton, R. S. Lieberman, and R. A. Vincent (1997), Climatology of the semiannual oscillation of the tropical middle atmosphere, *J. Geophys. Res.*, *102*, 26,019–26,032.
Garcia, R. R., D. R. Marsh, D. E. Kinnison, B. A. Boville, and F. Sassi (2007), Simulation of secular trends in the middle atmosphere, 1950–2003, *J. Geophys. Res.*, *112*, D09301, doi:10.1029/2006JD007485.
González-Galindo, F., M. A. López-Valverde, M. Angelats i Coll, and F. Forget (2005), Extension of a Martian general circulation model to thermospheric altitudes: UV heating and photochemical models, *J. Geophys. Res.*, *110*, E09008, doi:10.1029/2004JE002312.
Harada, Y., A. Goto, H. Hasegawa, N. Fujikawa, H. Naoe, and T. Hirooka (2010), A major stratospheric sudden warming event in January 2009, *J. Atmos. Sci.*, *67*, 2052–2069.
Hoffmann, C. G., U. Raffalski, M. Palm, B. Funke, S. H. W. Golchert, G. Hochschild, and J. Notholt (2011), Observation of strato-mesospheric CO above Kiruna with ground-based microwave radiometry—Retrieval and satellite comparison, *Atmos. Meas. Tech.*, *4*(11), 2389–2408, doi:10.5194/amt-4-2389-2011.
Hunton, D. E., A. A. Viggiano, R. A. Morris, and J. F. Paulson (1991), The $O^+ + CO_2$ reaction: New results and atmospheric implications, *J. Geophys. Res.*, *96*, 13,881–13,886.
Huestis, D. L., and J. Berkowitz (2010), Critical evaluation of the photoabsorption cross section of CO_2 from 0.125 to 201.6 nm at room temperature, in *Advances in Geosciences*, Planetary Science, vol. 25, pp. 229–242, World Scientific, Singapore.
Kaufmann, M., O. A. Gusev, K. U. Grossmann, R. Roble, M. E. Hagan, C. Hartsough, and A. Kutepov (2002), The vertical and horizontal distribution of CO_2 densities in the upper mesosphere and lower thermosphere as measured by CRISTA, *J. Geophys. Res.*, *107*(D23), 8182, doi:10.1029/2001JD000704.
Kunz, A., L. L. Pan, P. Konopka, D. E. Kinnison, and S. Tilmes (2011), Chemical and dynamical discontinuity at the extratropical tropopause based on START08 and WACCM analysis, *J. Geophys. Res.*, *116*, D24302, doi:10.1029/2011JD016686.
Lean, J., G. Rottman, J. Harder, and G. Kopp (2005), SORCE contributions to new understanding of global change and solar variability, *Sol. Phys.*, *230*, 27–53.
Lee, J. L., D. L. Wu, and A. Ruzmaikin (2013), Interannual variations of MLS carbon monoxide induced by solar cycle, *J. Atmos. Sol. Terr. Phys.*, *102*, 99–104.
Lindinger, W., F. C. Fehsenfeld, A. L. Schmeltekopf, and E. E. Ferguson (1974), Temperature dependence of some ionospheric ion-neutral reactions from 300–900 K, *J. Geophys. Res.*, *79*, 4753–4756.
Liu, H.-L., F. Sassi, and R. R. Garcia (2009), Error growth in a whole atmosphere climate model, *J. Atmos. Sci.*, *66*, 173–186.
López-Puertas, M., and F. W. Taylor (2001), *Non-LTE Radiative Transfer in the Atmosphere*, World Scientific, River Edge, N. J.
López-Puertas, M., M. A. López-Valverde, R. R. Garcia, and R. G. Roble (2000), A review of CO_2 and CO abundances in the middle atmosphere, in *Atmospheric Science Across the Stratopause*, *Geophys. Monogr. Ser.*, vol. 123, pp. 83–100, AGU, Washington, D. C.
López-Valverde, M. A., M. López-Puertas, J. J. Remedios, C. D. Rodgers, F. W. Taylor, E. C. Zipf, and P. W. Erdman (1996), Validation of measurements of carbon monoxide from the improved stratospheric and mesospheric sounder, *J. Geophys. Res.*, *101*, 9929–9956, doi:10.1029/95JD01715.
Marsh, D. R., M. E. Mills, D. E. Kinnison, J.-F. Lamarque, N. Calvo, and L. M. Polvani (2013), Climate change from 1850 to 2005 simulated in CESM1 (WACCM), *J. Clim.*, *26*, 7372–7391, doi:10.1175/JCLI-D-12-0558.1.
Matthes, K., U. Langematz, L. L. Gray, K. Kodera, and K. Labitzke (2004), Improved 11-year solar signal in the Freie Universität Berlin Climate Middle Atmosphere Model (FUB-CMAM), *J. Geophys. Res.*, *109*, D06101, doi:10.1029/2003JD004012.
Mertens, C. J., J. R. Winick, R. H. Picard, D. S. Evans, M. López-Puertas, P. P. Wintersteiner, X. Xu, M. G. Mlynczak, and J. M. Russell (2009), Influence of solar-geomagnetic disturbances on SABER measurements of 4.3 μm emission and the retrieval of kinetic temperature and carbon dioxide, *Adv. Space Res.*, *43*, 1325–1336.
Mlynczak, M. G., F. J. Martin-Torres, C. J. Mertens, B. T. Marshall, R. E. Thompson, J. U. Kozyra, E. E. Remsberg, L. L. Gordley, J. M. Russell III, and T. Woods (2008), Solar terrestrial coupling evidenced by periodic behavior in geomagnetic indices and the infrared energy budget of the thermosphere, *Geophys. Res. Lett.*, *35*, L05808, doi:10.1029/2007GL032620.
Nagy, A. F., T. E. Cravens, S. G. Smith, H. A. Taylor, and H. C. Brinton (1980), Model calculations of the dayside ionosphere of Venus: Ionic composition, *J. Geophys. Res.*, *85*, 7795–7801.
Ogawa, S., and M. Ogawa (1975), Absorption cross sections of O_2 ($a\,^1\Delta_g$) and O_2 ($X\,^3\Sigma_g^-$) in the region from 1087 to 1700 Å, *Can. J. Phys.*, *53*, 1845–1852.
Plane, J. M. C. (2004), A time-resolved model of the mesospheric Na layer: Constraints on the meteor input function, *Atmos. Chem. Phys.*, *4*, 627–638. [Available at http://www.atmos-chem-phys.net/4/627/2004/.]
Richter, J. H., F. Sassi, and R. R. Garcia (2010), Toward a physically based gravity wave source parameterization in a general circulation model, *J. Atmos. Sci.*, *67*, 136–156.
Rienecker, M. M., et al. (2011), MERRA: NASA's Modern-Era Retrospective Analysis for Research and Applications, *J. Clim.*, *24*, 3624–3648, doi:10.1175/JCLI-D-11-00015.1.

Rinsland, C., M. R. Gunson, R. Zander, and M. López-Puertas (1992), Middle and upper atmosphere pressure-temperature profiles and the abundances of CO_2 and CO in the upper atmosphere from ATMOS/Spacelab 3 observations, *J. Geophys. Res.*, *97*, 20,479–20,495.

Roble, R. G. (2000), On the feasibility of developing a global atmospheric model extending from the ground to the exosphere, in *Atmospheric Science Across the Stratopause*, *Geophys. Monogr. Ser.*, vol. 123, pp. 53–67, AGU, Washington, D. C.

Roble, R. G., and E. C. Ridley (1994), A thermosphere-ionosphere-mesosphere-electrodynamics general circulation model (TIME-GCM): Equinox solar cycle minimum simulations (30–500 km), *Geophys. Res. Lett.*, *21*, 417–420.

Sander, S. P., et al. (2011), Chemical kinetics and photochemical data for use in atmospheric studies, Evaluation No. 17, JPL Publ. 10-6, Jet Propul. Lab., Pasadena, Calif. [Available at http://jpldataeval.jpl.nasa.gov.]

Smith, A. K., R. R. Garcia, D. R. Marsh, and J. H. Richter (2011), WACCM simulations of the mean circulation and trace species transport in the winter mesosphere, *J. Geophys. Res.*, *116*, D20115, doi:10.1029/2011JD016083.

Solomon, S., and L. Qian (2005), Solar extreme-ultraviolet irradiance for general circulation models, *J. Geophys. Res.*, *110*, A10306, doi:10.1029/2005JA011160.

Thompson, B. A., P. Hartwick, and R. R. Reeves Jr. (1963), Ultraviolet absorption coefficients of CO_2, CO, O_2, H_2O, N_2O, NH_3, NO, SO_2, and CH_4 between 1850 and 4000 A, *J. Geophys. Res.*, *68*, 6431–6436.

Watanabe, K., and F. F. Marmo (1956), Photoionization and total absorption cross-section of gases. II. O_2 and N_2 in the region 850–1500 Å, *J. Chem. Phys.*, *25*, 965–971.

Weissler, G. L., and P. Lee (1952), Absorption coefficients of oxygen in the vacuum ultraviolet, *J. Opt. Soc. Am.*, *42*, 200–203.

Zaragoza, G., M. López-Puertas, M. A. López-Valverde, and F. W. Taylor (2000), Global distribution of CO_2 in the upper mesosphere as derived from UARS/ISAMS measurements (2000), *J. Geophys. Res.*, *105*, 19,829–19,839, doi:10.1029/2000JD900243.